Longitudinal assessment of lung cancer progression in the mouse using *in vivo* micro-CT imaging

Eman Namati[a)]
Department of Internal Medicine, University of Iowa, Iowa City, Iowa 52242 and School of Computer Science, Engineering and Mathematics, Flinders University, Adelaide 5042, Australia

Jacqueline Thiesse and Jessica C. Sieren
Department of Internal Medicine, University of Iowa, Iowa City, Iowa 52242 and Department of Biomedical Engineering, University of Iowa, Iowa City, Iowa 52242

Alan Ross
Department of Anesthesia, University of Iowa, Iowa City, Iowa 52242

Eric A. Hoffman
Department of Biomedical Engineering, University of Iowa, Iowa City, Iowa 52242 and Department of Radiology, University of Iowa, Iowa City, Iowa 52242

Geoffrey McLennan
Department of Internal Medicine, University of Iowa, Iowa City, Iowa 52242; Department of Biomedical Engineering, University of Iowa, Iowa City, Iowa 52242; and Department of Radiology, University of Iowa, Iowa City, Iowa 52242

Purpose: Small animal micro-CT imaging is being used increasingly in preclinical biomedical research to provide phenotypic descriptions of genomic models. Most of this imaging is coincident with animal death and is used to show the extent of disease as an end point. Longitudinal imaging overcomes the limitation of single time-point imaging because it enables tracking of the natural history of disease and provides qualitative and, where possible, quantitative assessments of the effects of an intervention. The pulmonary system is affected by many disease conditions, such as lung cancer, chronic obstructive pulmonary disease, asthma, and granulomatous disorders. Noninvasive imaging can accurately assess the lung phenotype within the living animal, evaluating not only global lung measures, but also regional pathology. However, imaging the lung in the living animal is complicated by rapid respiratory motion, which leads to image based artifacts. Furthermore, no standard mouse lung imaging protocols exist for longitudinal assessment, with each group needing to develop their own systematic approach.

Methods: In this article, the authors present an outline for performing longitudinal breath-hold gated micro-CT imaging for the assessment of lung nodules in a mouse model of lung cancer. The authors describe modifications to the previously published intermittent isopressure breath-hold technique including a new animal preparation and anesthesia protocol, implementation of a ring artifact reduction, variable scanner geometry, and polynomial beam hardening correction. In addition, the authors describe a multitime-point data set registration and tumor labeling and tracking strategy.

Results: *In vivo* micro-CT data sets were acquired at months 2, 3, and 4 posturethane administration in cancer mice (n=5) and simultaneously in control mice (n=3). 137 unique lung nodules were identified from the cancer mice while no nodules were detected in the control mice. A total of 411 nodules were segmented and labeled over the three time-points. Lung nodule metrics including RECIST, Ortho, WHO, and 3D volume were determined and extracted. A tumor incidence rate of 30.44 ± 1.93 SEM for n=5 was found with identification of nodules as small as 0.11 mm (RECIST) and as large as 1.66 mm (RECIST). In addition, the tumor growth and doubling rate between months 2–3 and 3–4 were calculated. Here, the growth rate was slightly higher in the second period based on the 3D volume data (0.12 ± 0.13 to 0.13 ± 0.17 μl) but significantly less based on the linear diameter metrics [RECIST (0.33 ± 0.19 to 0.17 ± 0.18 mm); Ortho (0.24 ± 0.15 to 0.16 ± 0.15 mm)], indicating the need to understand how each metric is obtained and how to correctly interpret change in tumor size.

Conclusions: In conclusion, micro-CT imaging provides a unique platform for *in vivo* longitudinal assessment of pulmonary lung cancer progression and potentially tracking of therapies at very high resolutions. The ability to evaluate the same subject over time provides for a sensitive assay that can be carried out on a smaller sample size. When integrated with image processing and analysis

I. INTRODUCTION

There are now many examples utilizing "micro" imaging modalities for the assessment of normal and diseased pulmonary phenotypes including micro-MRI for emphysema,[1,2] asthma,[3] and lung cancer;[4] micro-CT for emphysema,[5–8] pulmonary fibrosis,[9] and lung cancer;[10–15] micro-PET for lung cancer;[16,17] and recently, fluorescence molecular tomography for visualization of inflammation.[18]

Longitudinal pulmonary imaging in small animals, especially the mouse, is useful for tracking disease progression and the response of the disease process to potential therapies. However, very few longitudinal pulmonary studies have been presented to date using micromodalities. Froese *et al.*[6] presented serial micro-CT scans from Smad3 knockout mice and showed the superior utility of three-dimensional density measurements as opposed to two-dimensional and histologic assessment as a surrogate for development of airspace enlargement. Hori *et al.*[13] described the use of micro-CT for serial assessment of lung lesions in a mouse model of lung cancer and presented quantitative analysis of intrasubject tumor growth heterogeneity over a period of 20 weeks. Fushiki *et al.* presented the utility of micro-CT quantitative imaging for monitoring of lung cancer progression and suppression with confirmation using bioluminescence and histology.[12,19]

Performing longitudinal mouse lung imaging to provide valuable quantitative data in the microscale range (10–100 μm pixels) consistently can be difficult, as there are no standard mouse lung imaging protocols, with each group needing to develop and refine their own systematic approach. Micro-CT imaging is a useful modality for assessment of pulmonary structure in small animals, especially the mouse. Since micro-CT is an x-ray based imaging modality, if calibrated correctly the image content can be directly related to the density of the object under assessment. This fundamental property has been exploited for many years in clinical imaging, where it serves to qualitatively show, for instance, that muscle is different to bone or lung. Quantitative micro-CT scanning is now being employed in small animal micro-CT imaging for assessment of bone density, lung density, and cardiac output.[20]

Depending on the application and the technical requirements such as resolution, sensitivity, and acquisition speed, various forms of respiratory gating have been implemented. These include synchronous gating of an anesthetized free-breathing mouse[21] and prospective gating of intubated and ventilated mice at either end inspiratory, end expiratory,[10,11,22–24] or during controlled breath-holds.[25] Further, retrospective gating has been implemented during the reconstruction process[26–29] and recently, a retrospective phase-correlated approach where subject-specific optimization led to greater reduction of motion blurring.[30]

Recently, we introduced an intermittent isopressure breath-hold (IIBH) gating technique for *in vivo* imaging of the lung using a commercial micro-CT system.[31] In brief, the mouse is intubated, paralyzed, and ventilated using a computer controlled ventilator and x-ray projections are acquired during periodic breath-holds at user defined airway pressures. This approach provided high-resolution micro-CT imaging of an almost motion-free lung *in vivo* and has now been used by other groups with encouraging results.[25,32]

In this study, we present *in vivo* micro-CT imaging for longitudinal assessment of a lung cancer model and provide details for animal preparation, anesthesia, image acquisition, processing, and analysis. Investigation of a urethane induced mouse lung cancer model shows the unique ability of micro-CT imaging to identify and track individual lung nodule growth. As compared to previous studies describing the assessment of lung cancer, examples shown in this study have been evaluated at a very early stage due to the resolution advantage—Within 8 weeks of urethane administration for the lung cancer model. The implementation of the IIBH technique in conjunction with appropriate calibration and processing routines provided for a highly reproducible assay, enabling semiautomated segmentation and tracking of individual lung nodules over time. In addition, nodules could be accurately identified and related to their unique anatomical location such as their confining lobe, a feature that requires motion-free high-resolution imaging for segmentation of lobar fissure.

II. MATERIALS AND METHODS

II.A. Micro-CT imaging

A modified version of the IIBH micro-CT imaging technique, as described by Namati *et al.*,[31] was used for the longitudinal micro-CT scans in this study. In brief, the micro-CT x-ray source was set to 60 kVp and 500 μA tube current. The CCD detector was set to 500 ms exposure, binning of 2, and the system was configured to acquire 720 projections over 200° (half-scan) with 100 bright and dark calibration images. Each projection produced a 1536 $\times$ 1024 pixel image with a pixel spacing dimension of 28 $\times$ 28 μm^2. This protocol provides a MTF resolution at 10% of 55 μm. The MTF was calculated as previously described[31] using a 10 μm tungsten wire phantom (QRM, Nuremburg, Germany). Respiratory gating was performed using a combination of a computer controlled Flexivent (Scireq, Montreal, Quebec, Canada) ventilator, LABVIEW pro-

gram, and electronic solenoid triggering system. X-ray projections are essentially acquired at periodic breath-holds at a constant user defined airway pressure. Total scan time for each data set was 45 min.

II.B. Animal preparation

Experimental procedures carried out in this study had been approved by the University of Iowa Animal Care Committee.

II.B.1. Cancer mice

Normal A/J mice (n=8) aged between 6 and 8 weeks and weighing 20–22 g were used in this study. Each mouse was initially sedated using 3%–5% isofluorane, the mice were then weighed and n=5 were injected I.P. with 1 mg/g urethane (Sigma-Aldrich, St Louis, MO) dissolved in 0.9% NaCl saline. Mice were tagged with ear tags (Harvard Apparatus, Massachusetts, USA) and placed back into their respective cages to recover. As urethane is a known anesthetic agent, mice administered with urethane required approximately 30 min longer to regain consciousness.

Ethyl carbamate, the formal chemical name for urethane, was a common anesthetic agent used on animals. Once discovered to be the cause of lung adenomas in mice and rats, its use as an anesthetic agent diminished.[33] It was later proposed and demonstrated that vinyl carbamate epoxide, an oxidized off product of ethyle carbamate through two catalysations by the enzyme cytochrome P450 2E1, was the mutagenic and carcinogenic agent that would then react with DNA. The products of this reaction have miscoding properties and are considered the predominant source of the DNA lesions formed from ethyl carbamate.[34–37]

Prior to imaging, mice were initially sedated using 3%–5% isofluorane, weighed, and injected intramuscular (IM) in the right hind leg with 1.0 mg/kg medetomidine hydrochloride and 50.0 mg/kg ketamine. This anesthetic regiment was determined empirically in order to reduce total anesthesia while maintaining sufficient sedation for restraining mice during the intubation phase. Mice were intubated with a 22-gauge 1 in. Teflon catheter through the visual aid of a custom miniature fiber optic bronchoscope. Unlike previously described intubation techniques using a single optical fiber to illuminate the vocal chords,[38,39] here we constructed a flexible fiber optic bronchoscope using 10 000 optical fibers enabling clear visualization of the vocal chords through an external viewfinder. The fiber optic bronchoscope was constructed using a 0.45 mm 10 000 fiber image guide (Fujikura, Atlanta, GA) and a 0.35 mm/2 mm focal length GRIN lens (NSG, Somerset, NJ). The bronchoscope was fed through the 22-gauge catheter providing a unique ability to identify the trachea and feed the intubation tube over the bronchoscope. An image of the vocal chords of a mouse using the microbronchoscope is shown in Fig. 1. Clear identification of the vocal chords and trachea provides for swift placement of the intubation tube. A snake light was also placed under the chest resulting in light travel through the trachea to enable fast identification of the vocal chords.
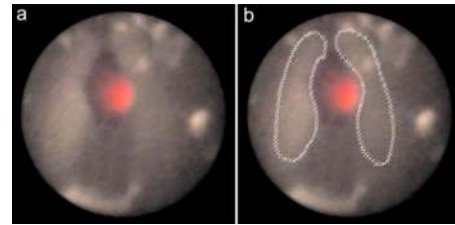

FIG. 1. (a) Example image using the microbronchoscope revealing the vocal chords of a mouse during intubation. (b) Dotted outline of vocal chords; the central glow is the diffusion of light through the chest cavity from an external snake light.

Triple antibiotic ointment was placed over the eyes to maintain moisture during the imaging phase, as the anesthesia inhibits spontaneous blinking. Mice were placed supine onto a polystyrene bed and mounted onto the micro-CT carbon fiber animal stage. The limbs were secured using tape and ECG and temperature sensors were attached for physiologic monitoring using a BioVet C1 data acquisition system (Supertron Technologies, Newark, NJ). Respiratory paralysis was achieved by administration of 0.5 mg/kg of rocuronium IM in the left hind leg. The tracheal catheter was then connected to a computer controlled Flexivent ventilator (Scireq, Montreal, Quebec, Canada) via 6 ft of 1/8 in. ID tubing. The mice were ventilated at 120 br/min and a tidal volume of 15 ml/kg. Isofluorane was set to 1%–2% for maintenance of sedation throughout the imaging protocol.

A heat lamp and cylindrical chamber was used to maintain body temperature between 35° and 37° centigrade during scanning to reduce hypothermia, which is a major contributor to mortality during anesthesia. Finally, 0.5 ml of PBS was injected subcutaneously above the abdomen in order to prevent dehydration during the imaging period.

We have now examined over 50 mice using the aforementioned protocol and found a decrease in mortality from approximately 30% to <10% after implementing the new anesthesia, temperature maintenance, and intubation approach. In addition, our recovery period decreased from 2 to 3 h postimaging when using ketamine and xylazine 87.5 mg/kg/12.5 mg/kg in combination with pancuronium 0.1 mg/g to 15–30 min when using ketamine and medetomidine 50.0 mg/kg/1 mg/kg with 0.5 mg/kg rocuronium as detailed above.

II.C. Image processing

Micro-CT images underwent several processing steps prior to reconstruction.

II.C.1. Ring artifact reduction

Ring artifacts are commonly observed in reconstructed micro-CT images due to the inconsistent signals between detector elements. The conventional approach for minimizing ring artifacts is a flat-field calibration step. Two sets of images are acquired to perform the flat-field calibration. A dark field is acquired with no x rays and represents the detector dark current and digitization noise while a bright field is acquired with the x rays on and provides an unattenuated
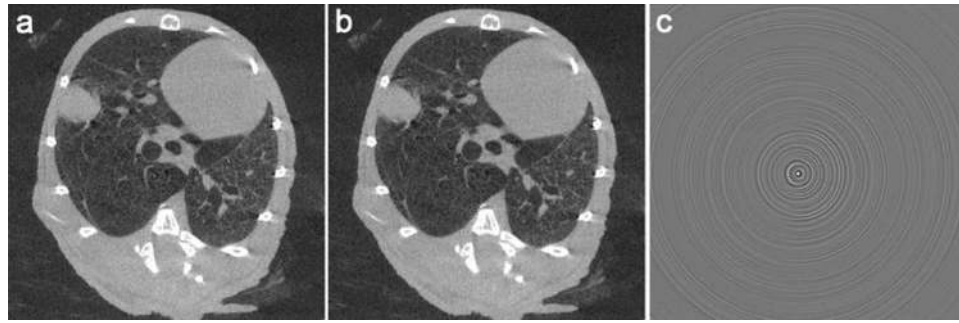
FIG. 2. (a) Reconstructed micro-CT image with no ring artifact reduction. (b) Sinogram low pass filtering ring artifact correction. (c) Difference image between (a) and (b).

projection. In this study, each projection x ray is log calibrated against a dark field and a bright field image acquired at the beginning of the scan. However, as these are normally acquired at the beginning of the scan, slight changes to the detector sensitivity over the duration of the mouse scan can result in ring artifacts in the reconstructed images. This effect is clearly evident if the system has not been allowed to reach a steady state temperature.

Several prereconstruction[40,41] and postreconstruction[42–44] techniques have been previously described. Here, we perform a prereconstruction low pass filtering step similar to Refs. 40 and 41 on the raw sinograms prior to reconstruction.

For each sinogram we calculate the average intensity profile across each row using

$$\overline{RS_x} = \frac{\sum_{\theta=0}^{n} S_{(x,\theta)}}{n}, \tag{1}$$

where RS_x is the average row sinogram value at column x. We then perform a low pass filter on this profile using a mean filter of length 9 and subtract this filtered version with the original averaged profile RS_x. The final profile which represents the difference of the average row sinogram profile and the smoothed sinogram profile is subtracted from every row in the sinogram. The filter width is related to the smoothing factor and preservation of object features. A value of 9 was found experimentally to result in a qualitative reduction of spikes representing line artifacts while preserving changes in object attenuation. Rivers described a similar technique[40] using a low pass filter in the Fourier domain and Boin *et al.*[41] using a moving average filter in the real space.

A reconstructed example of using only the flat-field calibration versus the addition of this filtering step is shown in Figs. 2(a) and 2(b), respectively. In addition, Fig. 2(c) represents the difference image between Figs. 2(a) and 2(b).

II.C.2. Variable geometry correction

The Siemens MicroCAT II incorporates a stationary specimen stage and a rotating source and detector couple. Imperfections in the gantry in addition to gravitational forces result in source-to-object-to-detector distance variations leading to suboptimal reconstructed images. Here we present a tech-

nique for determining this variation in terms of a dynamic center offset, source-to-object, and source-to-detector distance look up table that can be incorporated into the Feldkamp reconstruction algorithm (Exxim CC, Pleasanton, CA). The lookup table was created using a custom 12.7 mm brass ball bearing phantom scanned using the *in vivo* imaging protocol outline above. The projection images were processed and the area of the ball was converted into a translational shift versus projection angle. The area-to-translational shift was calculated using a prior calibration step that included acquiring images of the ball bearing phantom at two known relative distances and applying the concept of similar triangles as illustrative in Fig. 3.

Here, a is the known ball phantom diameter, d is the known translation of the phantom toward the detector, and finally the known detector pixel dimension is used to calculate b_1 and b_2. Using similar triangles, x and y are calculated using the following equations:
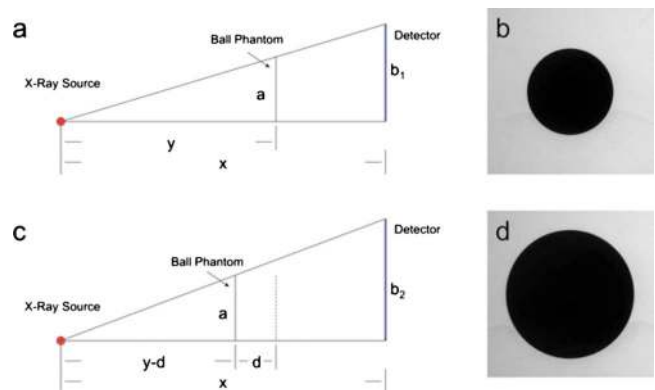
$$y = \frac{b_2 d}{b_2 - b_1}, \tag{2}$$

FIG. 3. [(a) and (c)] Schematic geometric illustration for calculating the source-to-object and source-to-detector distance using the ball bearing phantom x-ray projections at two known distances. Ball phantom x-ray projection, (b) position 1: Closer to detector; (d) position 2: Closer to source.
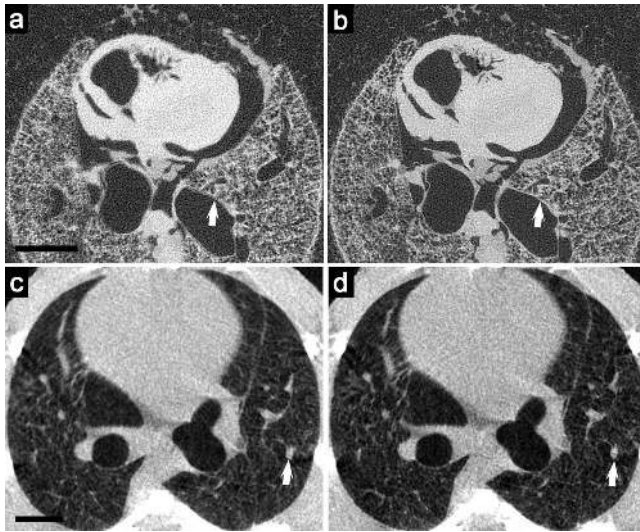
FIG. 4. (a) Standard reconstruction and (b) reconstruction using a dynamic center offset, source-to-object, and source-to-detector distance look up table. The arrow indicates a region that is significantly improved using the dynamic lookup tables. Scale bar=2 mm.

$$x = \frac{\dfrac{b_1 b_2 d}{b_2 - b_1}}{a}. \tag{3}$$

The value for the center offset, source-to-object, and source-to-detector distance was calculated for each angle and averaged over ten complete scans. A standard deviation of 0.473 mm was measured for the translation shift (mm) from the piercing point over 360°. The mean of the standard deviation across ten scans for the translation shift at each corresponding angle was measured to be 0.0141 mm, indicating the reproducibility of the shift between scans. An example of the result using the dynamic center offset, source-to-object, and source-to-detector distance reconstruction for both an *ex vivo* fixed and *in vivo* breath-hold lung data set are illustrated in Figs. 4(a) and 4(b) and Figs. 4(c) and 4(d), respectively. Here

the fixed sample was scanned with a binning of 1 resulting in a reconstructed pixel dimension of 14×14 μm^2 and illustrates the improvement while eliminating motion related effects. The difference between the *in vivo* images is subtle, but still evident as indicated by the arrows to the vessel.

II.C.3. Beam hardening correction

Beam hardening is a common problem associated with the use of a polychromatic x-ray source. When performing quantitative analysis of density and, in particular, regional differences in density within and across subjects, reducing the effects of beam hardening are important. In addition to a hardware filter (e.g., 0.5 mm aluminum plate), there are also several computational techniques that have been previously introduced to reduce beam hardening. The simplest is a widely implemented *a priori*, nonlinear polynomial correction.[45] This approach was implemented here using a custom 10, 20, and 30 mm water equivalent cylindrical phantom. The phantom was scanned using the *in vivo* imaging protocol outline above and a third order polynomial was fit to the x-ray attenuation versus thickness. These coefficients were then used in combination with the EXXIM Cobra (Exxim CC, Pleasanton, CA) reconstruction algorithm. Figure 5 represents the density line profile across the center of the 10, 20, and 30 mm phantom in the axial plane (a) before and (b) after correction. A second order polynomial regression for each reveals a clear improvement in the corrected versus noncorrected profiles. Here the R^2 value was 0.1213, 0.1890, and 0.2231 versus 0.0445, 0.0002, and 0.0239 for the corrected. Subjectively, we can see the density profiles for the different size cylinders have been flattened and the difference in the average density between the profiles has been reduced.

II.C.4. Hounsfield unit calibration

The attenuation values from reconstructed micro-CT images were calibrated and scaled into Hounsfield units (HU) by ensuring that water is 0 HU and air is −1000 HU. At-
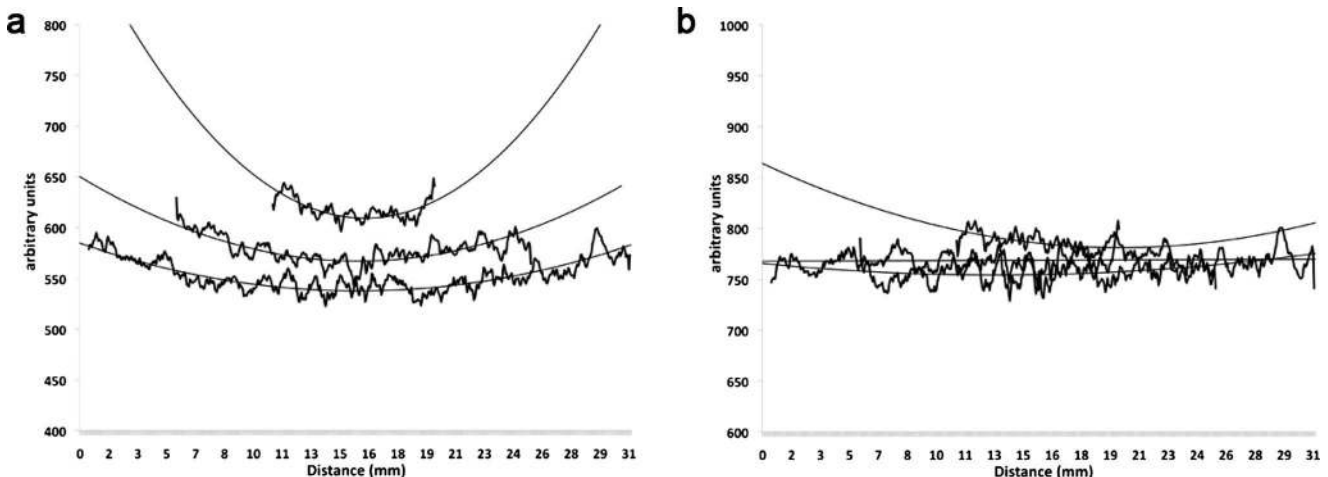

FIG. 5. Density line profile across the center of a 10, 20, and 30 mm beam hardening phantom in the axial plane (a) before and (b) after beam hardening correction.

tenuation values representing each pixel were initially normalized and truncated into integer values by the following expression:

$$CT(x,y) = \frac{\mu(x,y) - \mu\text{water}}{\mu\text{water}} \times 1000, \qquad (4)$$

where $\mu(x,y)$ represents the high precision floating point attenuation number for each pixel (x,y) before conversion, $CT(x,y)$ is the CT number in Hounsfield units, and μwater is the attenuation coefficient for water.

HU calibration and scaling was performed using a water equivalent plastic phantom prior to each imaging session. Calibration into HU provides a convenient scale for segmentation and assessment of tissue with unique density values. In addition, HU calibrations allows for quantitative comparison between data sets and time-points.

II.C.5. Longitudinal lung registration

Registration between multiple time-point *in vivo* micro-CT data sets was performed using the AMIRA VISUALIZATION software platform. Data sets were registered through an iteratively optimized rigid transformation process based on mutual information. Registration was performed on the entire data set in three dimensions; however, only voxels bound between −1024 and 500 HU were sampled for calculating the mutual information. This reduced the bias due to high contrast structures other than the lung, such as the ribs and spine (1000HU+). The registration process was performed iteratively by varying the resampling factor of the reference data set from 16× to 1×. After each iteration, the previously calculated coordinate transform (three translation and three rotation parameters) of the model data set was used as the starting point for the next optimization. The final registered data sets was then resampled into the reference lattice using a Lanczos interpolation algorithm and finally exported as RAW 16 bit images.[46] A flow diagram of this process is shown in Fig. 6. In all cases, the second time-point data set was used as the reference for registration.

II.C.6. Tumor segmentation

In vivo micro-CT image data sets were imported into a prototype oncology program (OncoCare, Siemens, NJ, USA). Tumors were located manually and traced using a semiautomated segmentation routine.[47,48] First a straight line or stroke across the cross-section of the tumor was drawn, keeping each end of the line close to the boundary of the tumor. The program then automatically performs three main
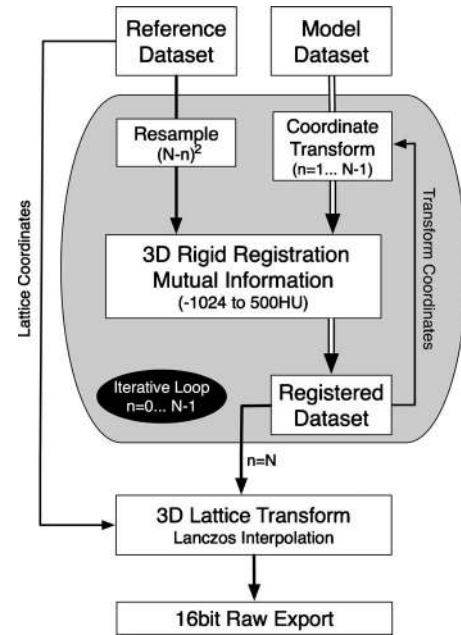

FIG. 6. Rigid registration flow diagram for registering multitime-point micro-CT data sets to one another.

tasks. First, the algorithm learns the rough gray level distribution of the lesion from the stroke using a multiregion fuzzy connectedness algorithm. Second, the lesion is segmented on the current 2D plane and on 2D planes orthogonal to it using a shortest path algorithm. At the end of each segmentation, the gray level distribution for the lesion and the background is calculated and fed back into the algorithm. Finally, a random walker algorithm utilizing the seeds generated from the 2D segmentations are used to compute the 3D segmentation. Here, the algorithm determines the probability that a random walker initiating its walk from each voxel first arrives at a lesion seed before arriving at a background seed. The automated tracings were then manually inspected and borders were altered, as needed, using a series of manual tools.

Each tumor was given a unique label as shown in Table I.

As an example, RL3_4_P would represent the fourth nodule located in the right caudal lobe adjacent to the pleura. Identification of anatomical structures such as lobar fissures provides a powerful means for compartmentalizing results for regional assessment of tumor incidence and growth rate.

Multiple size metrics for each segmented tumor were exported for further analysis, including tumor diameter based

TABLE I. Nodule labeling nomenclature.

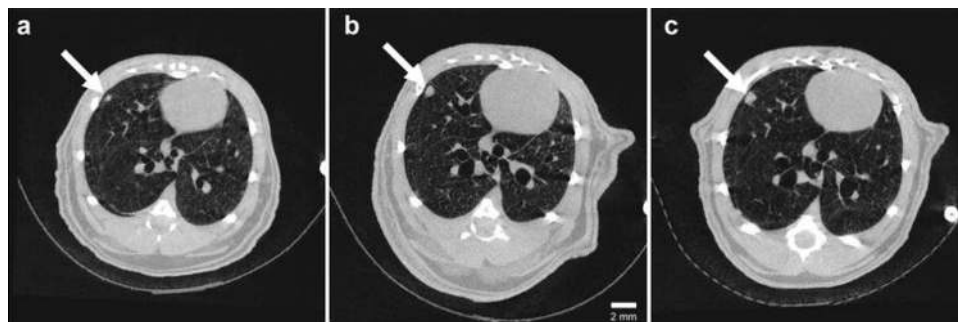| Confining lobe	Anatomical position	Special attributes
RL1=right cranial lobe	S=solitary	A=nodule surrounded by atelectasis
RL2=right accessory lobe	H=heart	D=nodule has disappeared
RL3=right caudal lobe	P=pleura	
RL4=right middle lobe	L=lobe fissure	
LL1=left lung		

FIG. 7. Axial images from the same urethane induced A/J mouse at 2, 3, and 4 months posturethane administration, acquired using the *in vivo* micro-CT imaging technique. A growing pulmonary nodule located in the right azygous lobe can be identified at each time-point as indicated with the arrow (window=3000, level=250).

on the Response Evaluation Criteria in Solid Tumors (RE-CIST) (14–16), orthogonal (Ortho) tumor diameter, the World Health Organization (WHO) response criteria (14–16), 3D tumor volume, mean tumor HU density of voxels within the volume, and standard deviation of HU density within each tumor volume. This data was exported and formatted for further statistical analysis using SPSS (SPSS Inc., Chicago, IL).

The WHO criterion provides a bidimensional metric based on the product of the maximum diameter in an axial image by the largest perpendicular diameter in the same image, the RECIST criteria provides a unidimensional metric using the largest diameter in a single plane, while the Ortho metric provides the maximum orthogonal diameter. In the two later cases measurements are a diameter value and commonly limited to the transverse plane.

II.D. Intraobserver and interobserver study

To assess the reproducibility and variation in measuring tumor metrics using the aforementioned segmentation tools, intraobserver and interobserver studies were carried out. Each observer (n=3) segmented tumors (n=32) from a single mouse at the final time-point using the semiautomated algorithm. The original expert observer also retraced the tumors from the same data set two additional times in two different sittings separated by a period of three weeks.

Tumor labels across the observers and sittings were consolidated and statistical analysis was undertaken to determine the reliability of repeated measures. The intraclass correlation coefficient (ICC) and coefficient of variation (CV) were determined for both the intraobserver and interobserver results and shown in Tables IV and V, respectively.

III. RESULTS

III.A.1. Lung cancer four-month three-time-point study

Micro-CT data sets from each urethane induced A/J mouse scanned at 2, 3, and 4 months posturethane administration were registered with one another as outlined in the

methods. Axial images revealing the progressive growth of a pulmonary nodule for one of the urethane mice are shown in Fig. 7.

Using the registered *in vivo* micro-CT data sets of the same urethane induced A/J mouse at 2, 3, and 4 months, individual tumors were segmented using a semiautomated approach and visualized as shown in Fig. 8.

Quantification of segmented tumors as shown in Fig. 8 was undertaken and common tumor metrics including the RECIST, Ortho, WHO, and 3D volumes were extracted. The RECIST, Ortho, WHO, 3D diameter, and 3D volume measurements for three out of a total of 31 nodules for one urethane induced A/J mouse have been plotted in Figs. 9(b)–9(f), respectively. A combined graph including the RE-CIST, Ortho, WHO, and 3D diameter has also been generated in Fig. 9(a). The 3D diameter was calculated based on the measured 3D volume and provides a "linear" representation for comparative purposes. In addition, the standard de-
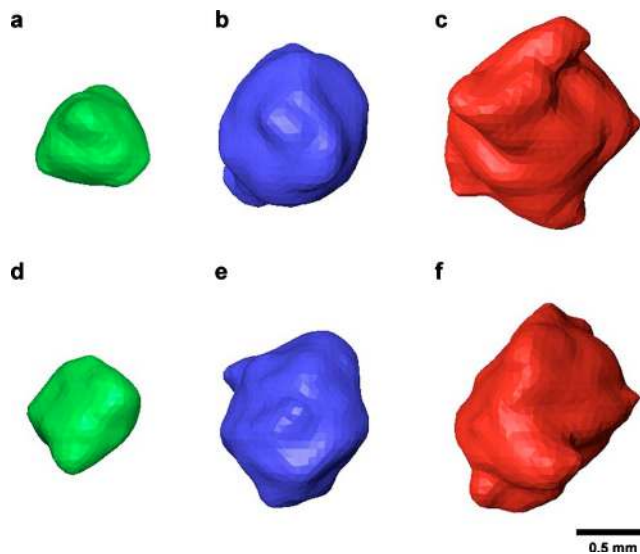

FIG. 8. [(a), (b), (d), and (f)] Axial and coronal three-dimensional reconstructions of a mouse lung tumor (RL2_2_P) as identified at 2, 3, and 4 months posturethane administration, respectively.
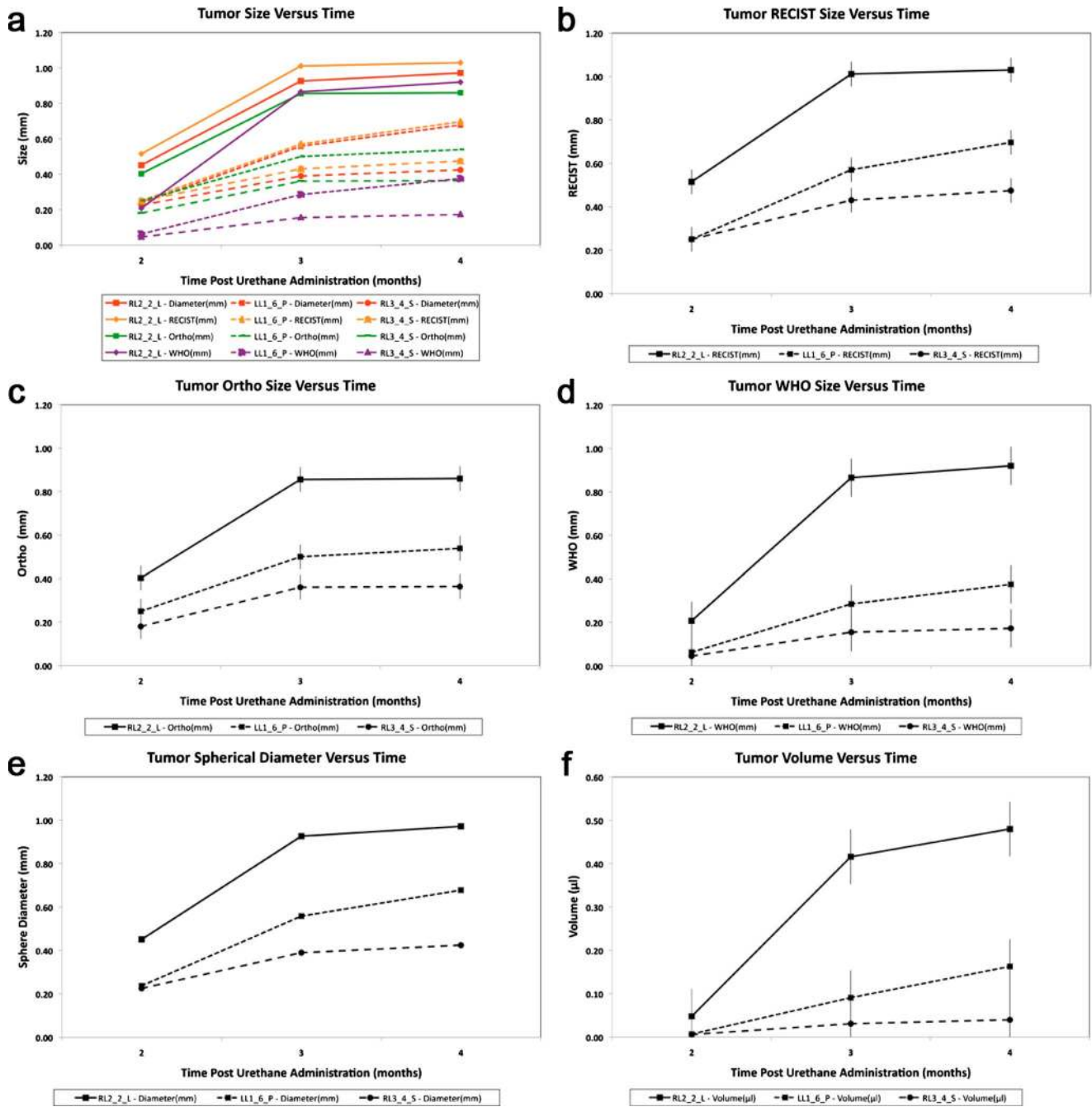
FIG. 9. (b) RECIST (mm), (c) Ortho (mm), (d) WHO (mm^2), (e) 3D diameter, and (f) 3D volume (μl) growth rate for the tumor shown in Fig. 8 plus two out of the 31 total tumors from the same mouse. (a) Combined RECIST, Ortho, WHO, and 3D diameter growth rates. Error bars represent the $\pm$ standard deviation from the intraobserver study for each metric, respectively.

viation from the intraobserver study for each metric are shown as error bars for the RECIST, Ortho, WHO, and 3D volume graphs.

Table II represents an overview of the statistics for tumors identified and tracked over months 2, 3, and 4 posturethane administration in lung cancer mice (n=5). 137 unique lung nodules were identified and a total of 411 nodules were segmented and labeled over the three-time-point study. Nodules as small as 0.11 mm and as large as 1.66 mm were identified and segmented. A mean RECIST (mm), Ortho (mm), WHO (mm^2), and 3D Volume (μl) of 0.65 ± 0.01, 0.48 ± 0.01,

0.36 ± 0.02, and 0.13 ± 0.01 (SEM) were measured, respectively, from all tumors across all mice over the three time-points.

Table III represents an overview of the tumor growth and doubling rates from all nodules tracked over months 2, 3, and 4 posturethane administration in lung cancer mice (n =5). The mean and standard deviations for growth and doubling rates have been calculated for each segment, i.e., months 2–3 and 3–4 for each metric.

Tables IV and V represent the results for the intraobserver and interobserver study, respectively. Here, the intraclass

TABLE II. Overview of lung nodule metrics for identified and tracked nodules over months 2, 3, and 4 posture-thane administration for n=5 mice.

Scan month		Volume (μl)	RECIST (mm)	Ortho (mm)	WHO (mm²)	HU (mean)	HU (std)
Month 2, N=137	Mean	0.025	0.384	0.278	0.121	−299	126
	Std. error of mean	0.004	0.019	0.016	0.014	23	4
	Minimum	0.003	0.112	0.101	0.020	−653	56
	Maximum	0.212	0.860	0.711	0.611	36	216
Month 3, N=137	Mean	0.110	0.640	0.461	0.329	−242	158
	Std. error of mean	0.012	0.022	0.018	0.024	16	4
	Minimum	0.003	0.250	0.141	0.035	−560	71
	Maximum	0.571	1.204	0.922	1.031	116	250
Month 4, N=137	Mean	0.206	0.773	0.584	0.502	−206	176
	Std. error of mean	0.022	0.023	0.020	0.034	15	5
	Minimum	0.003	0.180	0.158	0.033	−690	78
	Maximum	1.515	1.664	1.373	2.285	176	411

correlation coefficient and the coefficient of variation have been calculated and presented for the segmentation and measurement of 32 tumors. Table IV was compiled from the repeated measures (n=3) from an expert observer while Table V was compiled from the single execution by three different observers.

IV. DISCUSSION

Many disease conditions generate negative implications on normal lung structure and function, yet comprehensive longitudinal assessment of this organ is difficult because of its heterogeneity and significant motion *in vivo*. In this paper, we have presented a new methodology for longitudinal micro-CT lung imaging and associated quantitative descriptions and have applied these successfully to tracking the growth of lung nodules in a mouse model of lung cancer.

In our previous paper describing the IIBH technique, the reproducibility of measuring lung volume and air fraction using lung density was assessed in the same mice through acquisition and analysis of multiple micro-CT scans for four different gating techniques. Based on the two standard deviation Bland–Altman analysis, the IIBH technique was found to be more reproducible for both lung volume (38.13 μl versus 11.9 μl) and air content (13% versus 3.1%) metrics for nongated versus IIBH gating, respectively. In addition,

the short-term reproducibility of both the image acquisition using the IIBH technique and image analysis based on calibrated HU density values were presented.[31]

This previous study provided a good foundation for the longitudinal assessment of tumor size using the semiautomated segmentation approach carried out here. Both the lung volume and density are important features that affect both the real tumor size and the tumor segmentation algorithm described in Sec. II. In particular, when a user selects a region of interest by drawing a line across the tumor, the algorithm first uses the different density information to determine the correct seed locations for the lesion versus normal tissue. Based on this approach, it is critical that lung density values are reproducible across time-points. In addition, differences in lung volume can clearly affect the real tumor size due to distending forces from the surrounding parenchyma at different volumes or inflation pressures. Therefore, maintenance and reproducibility of lung volume and density are of primary concern for semiautomated tumor size measurements across time-points.

In this study, significant development was undertaken to the anesthesia and animal preparation protocols, where both the mortality and efficient recovery of the mouse postimaging were critically important for longitudinal imaging. A review of established anesthesia procedures[49–51] as well as em-

TABLE III. Tumor growth and doubling rate from nodules over months 2, 3, and 4 posturethane administration for n=5 mice.

		Volume (μl)	RECIST (mm)	Ortho (mm)	WHO (mm²)
Growth rate, months 2–3	Mean (per month)	0.124	0.336	0.249	0.292
	Std deviation	0.138	0.198	0.153	0.234
Growth rate, months 3–4	Mean (per month)	0.131	0.178	0.169	0.236
	Std deviation	0.174	0.182	0.152	0.268
Doubling rate, months 2–3	Mean (months)	1.3	2.3	2.2	1.3
	Std deviation	1.6	2.2	1.0	1.2
Doubling rate, months 3–4	Mean (months)	1.2	13.9	6.5	5.0
	Std deviation	4.9	85.3	28.6	18.6

TABLE IV. Intraobserver intraclass correlation coefficient and coefficient of variation results for repeated (n =3) segmentation and measurement of tumors (n=32) by the same observer.

Variable	Mean	ICC		CV (%)	
		Estimate	95% CI	Estimate	95% CI
Volume (μl)	0.271	0.97	(0.94,0.98)	23.1	(19.7,27.9)
RECIST (mm)	0.826	0.97	(0.95,0.99)	6.8	(5.8,8.2)
Ortho (mm)	0.621	0.96	(0.93,0.98)	9.1	(7.8,11.0)
WHO (mm^2)	0.602	0.97	(0.95,0.99)	14.6	(12.4,17.6)

pirical testing was undertaken. In particular, the IIBH technique required paralysis of the mouse for stable breath-hold periods. Here rocuronium was utilized as opposed to pancuronium as the half life was much shorter ($\sim$60 vs $\sim$200 min). This allowed for faster recovery (15–30 min as opposed to 2–3 h) and spontaneous breathing postmicro-CT scanning. In addition, mice were intubated and therefore required a short acting general anesthetic and analgesic that would cover both the intubation phase and the animal preparation period. Here we used a combination of medetomodine hydrochloride and ketamine. Medetomidine was utilized as opposed to xylazine, due to its higher affinity for alpha-2 receptors and the availability of a reversal agent (atipamezole) for fast postrecovery. A custom built microbronchoscope was also constructed in order to aid in fast and minimal risk intubations. Finally, maintaining an optimal body temperature during imaging increased the metabolism of the anesthetic and paralytic agents aiding in fast postrecovery. This combination of animal preparation and anesthesia resulted in a lower mortality ($<$10% as opposed to $\sim$30%), enabling high-resolution breath-hold imaging for longitudinal studies.

Although reconstructed images are, by their nature, artificial, practical steps can be taken to reduce inconsistencies and artifacts associated with micro-CT images within and across specimens. Such steps are paramount if quantitative analysis is to be made with a degree of certainty. Here we presented additional processing steps including ring artifact reduction, variable scanner geometry correction, and polynomial beam hardening correction to increase the resolution and consistency of the reconstructed images. With the ubiq-uitous use of micro-CT systems for research, such steps are now either available or will become standard features in commercial systems.

The prereconstruction ring artifact correction approach was chosen as opposed to postreconstruction techniques through qualitative assessment of the final reconstructed image and quantitative comparison of processing time. It was found that using a mean filter on the average row sinogram profile provided both a fast and effective approach as opposed to a Fourier domain low pass filtering step as previously described by Rivers,[40] which also induced additional artifacts due to the Gibbs phenomenon. A similar result was also described by Boin *et al.*[41] who found that filtering in the real space provided for qualitatively better images.

Cone beam computed tomography (CBCT) has become a well established technique for portable tomographic imaging in the clinical setting. Previous studies have described geometric calibration techniques for C-arm systems to improve reconstructed images.[52,53] The EXXIM reconstruction platform used in the Siemens micro-CAT II system was originally designed for C-arm CBCT reconstruction and has several features that are not utilized in the Siemens micro-CT user interface. Here we describe a simple technique to create the dynamic source-to-object, source-to–detector, and center offset lookup tables for integration with the EXXIM reconstruction platform. Although the Siemens gantry proved to be quite stable with less than 1 mm of shift at the piercing point, an improvement in images acquired from a fixed sample can be appreciated as illustrated in Figs. 4(a) and 4(b). A fixed sample was used here to eliminate the effects of motion providing a better comparison for illustrative purposes. The ben-

TABLE V. Interobserver intraclass correlation coefficient and coefficient of variation results for segmentation and measurement of tumors (n=32) by three observers.

Variable	Mean	ICC		CV (%)	
		Estimate	95% CI	Estimate	95% CI
Volume (μl)	0.260	0.95	(0.90,0.97)	30.5	(26.0,36.9)
RECIST (mm)	0.813	0.95	(0.91,0.97)	9.0	(7.7,10.9)
Ortho (mm)	0.606	0.95	(0.91,0.97)	10.6	(9.0,12.8)
WHO (mm^2)	0.580	0.96	(0.92,0.98)	18.6	(15.5,21.9)

efits of using this geometric correction on the *in vivo* data sets were subtle but still evident as shown in Figs. 4(c) and 4(d). Once the lookup table has been calculated, there is limited overhead in performing the reconstruction with the geometric correction.

Investigation of lung cancer at an early stage is of great importance, as our understanding of the early progression of this disease is limited. Evaluation of mouse models of lung cancer have provided further understanding of the genetic processes involved that lead to known phenotypes.[54,55] The ability to assess the same lung tumor from a very early stage *in vivo* using micro-CT imaging will enable a new approach to experimental studies. Here we have shown the utility of micro-CT imaging to identify and track individual tumor growth rates with high spatial resolution. Through implementation of a 3D rigid registration process, nodules could be confidently identified across time-points. Using a prototype oncology package, tumors were successfully segmented and important metrics were extracted, including the 3D volume for each nodule.

From the RECIST and Ortho growth plots in Figs. 9(b) and 9(c), we can see that although the nodule shown in Fig. 7 (RL2_2_L) does not appear to have grown between months 3 and 4, the multidimensional WHO data in Fig. 9(d), and more prominently the volumetric measurement and plot in Fig. 9(f), reveal a clear increase in size over this period. Furthermore, the three-dimensional reconstruction (Fig. 8) of the tumor clearly presents the increasing size when visualized as a volume.

The 3D diameter Fig. 9(e) was calculated based on the 3D volume to provide a linear measure for comparison to the RECIST and Ortho metrics as shown in Fig. 9(a). Since we expect the tumors in this model at the sizes reported here to be spherical, it is not surprising that the 3D diameter is comparable to the RECIST and Ortho metrics. However, in the case of nonspherical tumors, we would expect that the 3D volume and 3D diameter value to be significantly different to the RECIST and Ortho metrics, with the volume measures providing greater sensitivity.

A mean overview of the tumors identified and tracked in this study is presented in Table II. Here we can identify the smallest and largest nodule measured to be 0.11 and 1.66 mm, respectively, using the RECIST criteria. It can also be seen that the mean Hounsfield value is increasing over months 2, 3, and 4 indicating the tumors are becoming more solid. In addition, the standard deviation is increasing over this period, revealing a greater intratumor and/or intertumor tissue heterogeneity. Tumor growth and doubling rates were also calculated for each tumor across all mice with the average and standard deviation reported in Table III. The tumor growth rate based on the volume measures shows a slight increase between months 2–3 (0.12 ± 0.13 μl) and 3–4 (0.13 ± 0.17 μl), while the RECIST (0.33 ± 0.19 to 0.17 ± 0.18 mm), Ortho (0.24 ± 0.15 to 0.16 ± 0.15 mm), and WHO (0.29 ± 0.23 to 0.23 ± 0.26 mm^2) measures all show a decrease in growth rate between the same periods. The doubling rate reveals a similar trend, where the rate is decreasing for the volume measure and increasing for the RECIST, Ortho, and WHO measures. In addition, the doubling rate, which is a normalized value of time but not size, is quite different across the metrics particularly for the second period. This is most evident when comparing the volume versus the RECIST and Ortho measures. The underestimation of the growth rate using the unidimensional metrics is quite evident from these results and reveals the greater sensitivity of volume measurements for this task. However, it should be noted, as reported and discussed below, that volume measures are also more sensitive to observer and/or segmentation variability.

The reliability of the semiautomated segmentation approach for measuring lung nodules was found to be very high based on the intraclass correlation coefficient for both the interobserver (>0.96) and intraobserver (>0.95) studies as shown in Tables IV and V. This was not surprising as the algorithm was quite robust and the two additional observers were trained by the expert observer prior to the study to identify and segment tumors. The coefficient of variation reveals the increased sensitivity of both the volume (23.1% and 30.5%) and WHO (14.6% and 18.6%) metrics versus the linear RECIST (6.8% and 9.0%) and Ortho (9.1% and 10.6%) for the intraobserver and interobserver studies, respectively. This increased sensitivity using such two-dimensional and three-dimensional metrics further emphasizes the importance of understanding how each metric is obtained and the increasing sensitivity of the measures due to segmentation/observer variability as the dimensionality increases. Overall, these results still indicate the strong reproducibility of using the image analysis technique described in this study to measure lung nodules.

In a previous paper describing longitudinal assessment of lung nodules in mice using micro-CT imaging,[56] the smallest identifiable nodule documented was approximately 0.2 mm without the use of respiratory gating. In a more recent study by Hori *et al.*,[13] the smallest nodule identified was 0.5 mm using synchronized respiratory gating and cast doubt over the minimum size detectable as documented in the previous study with no gating. Here, using the breath-hold gating technique, we were able to identify nodules down to 0.11 mm (RECIST) in diameter although the majority of initial nodules were detected at >0.20 mm, clearly providing a major advantage for assessment of lung nodules at a very early stage.

A fundamental advantage of using the IIBH technique for high-resolution lung imaging is the ability to identify structures of interest at an earlier stage. Here we have performed assessment of the urethane induced lung cancer model at significantly earlier stages to previous studies. Garbow *et al.*[4] began assessment of Urethane induced tumor mice at 8 months posturethane administration, Hori *et al.*[13] began at 10 weeks posturethane administration, while here we present identification and tracking of nodules at 8 weeks posturethane administration. Also, both prior studies identified less than three times the average number of lesions as found in

previous histologic examinations of the same model.[57] While here in this study, we found similar tumor incidence rates of 20–40 per mouse (30.44 ± 1.93 SEM, n=5).

Radiation dose is an important factor when planning and executing micro-CT imaging and more so when undertaking longitudinal assessment of disease progression. Each scan performed in the study presented here administered approximately 0.85 Gy of radiation to the mouse as calculated using the Siemens dosage calculator. Mole had previously reported that mice can neutralize daily whole-body doses between 0.25 and 0.5 Gy.[31,58] However, those experiments were performed on CBA mice while A/J mice were used in this study. In addition, the criterion for neutralization was that of survival rather than implying complete restoration to the *status quo ante*.[59] A study by Safwat *et al.*[60] measured the radiation-induced lung damage threshold for mice between 12 and 15.8 Gy with a greater threshold for lower rates of dosage administration (0.71 versus 0.08 Gy/min). Sequential radiation therapy has also been reported in the order of five 10 Gy daily doses.[61] Carlson *et al.* recently presented a study on radiation dose due to micro-CT imaging on subcutaneous and simulated internal tumors. They concluded that the dosage levels were likely below the threshold to affect tumor growth using their ultrafast protocol; however, further investigation into other imaging protocols such as those presented here need to be undertaken. Based on these findings along with our low dosage rate of 0.018 Gy/min, we do not expect adverse or therapeutic effects on the mice or lung tumors in this longitudinal study; however, considering the differences in sensitivity between mice strains and lung cancer models, further studies should be undertaken in order to characterize potential dosage effects.

In conclusion, micro-CT imaging provides a unique platform for *in vivo* longitudinal assessment of lung cancer progression at very high resolutions. In addition, the ability to evaluate the same subject over time provides for a sensitive assay that can be carried out on a smaller sample size. When integrated with image processing and analysis routines as detailed here, the data acquired from micro-CT imaging can now provide a very powerful assessment of pulmonary disease progression.

ACKNOWLEDGMENTS

[a])Author to whom correspondence should be addressed. Electronic mail: eman-namati@uiowa.edu.

[1]L. E. Olsson *et al.*, "Measurement of MR signal and $T2^*$ in lung to characterize a tight skin mouse model of emphysema using single-point imaging," J. Magn. Reson Imaging **25**(3), 488–494 (2007).

[2]B. Driehuys and L. W. Hedlund, "Imaging techniques for small animal models of pulmonary disease: MR microscopy," Toxicol. Pathol. **35**(1), 49–58 (2007).

[3]B. Driehuys *et al.*, "3He MRI in mouse models of asthma," Magn. Reson.

Med. **58**(5), 893–900 (2007).

[4]J. R. Garbow *et al.*, "Quantitative monitoring of adenocarcinoma development in rodents by magnetic resonance imaging," Clin. Cancer Res. **14**(5), 1363–1367 (2008).

[5]N. L. Ford *et al.*, "Quantifying lung morphology with respiratory-gated micro-CT in a murine model of emphysema," Phys. Med. Biol. **54**(7), 2121–2130 (2009).

[6]A. R. Froese *et al.*, "Three-dimensional computed tomography imaging in an animal model of emphysema," Eur. Respir. J. **30**(6), 1082–1089 (2007).

[7]M. Kawakami *et al.*, "Sequential and quantitative analysis of a murine model of elastase-induced emphysema," Biol. Pharm. Bull. **31**(7), 1434–1438 (2008).

[8]A. A. Postnov *et al.*, "*In vivo* assessment of emphysema in mice by high resolution x-ray microtomography," J. Microsc. **220**, 70–75 (2005).

[9]S. Shofer *et al.*, "A micro-computed tomography-based method for the measurement of pulmonary compliance in healthy and bleomycin-exposedmice," Exp. Lung Res. **33**(3–4), 169–183 (2007).

[10]D. Cavanaugh *et al.*, "*In vivo* respiratory-gated micro-CT imaging in small-animal oncology models," Mol. Imaging **3**(1), 55–62 (2004).

[11]D. D. Cody *et al.*, "Murine lung tumor measurement using respiratory-gated micro-computed tomography," Invest. Radiol. **40**(5), 263–269 (2005).

[12]H. Fushiki *et al.*, "Quantification of mouse pulmonary cancer models by microcomputed tomography imaging," Cancer Sci. **100**(8), 1544–1549 (2009).

[13]Y. Hori *et al.*, "Periodic analysis of urethane-induced pulmonary tumors in living A/J mice by respiration-gated x-ray microcomputed tomography," Cancer Sci. **99**(9), 1774–1777 (2008).

[14]M. J. Paulus *et al.*, "High resolution x-ray computed tomography: An emerging tool for small animal cancer research," Neoplasia **2**(1-2), 62–70 (2000).

[15]R. Savai *et al.*, "Evaluation of angiogenesis using micro-computed tomography in a xenograft mouse model of lung cancer," Neoplasia **11**(1), 48–56 (2009).

[16]V. Ambrosini *et al.*, "Assessment of a chemically induced model of lung squamous cell carcinoma in mice by 18F-FDG small-animal PET," Nucl. Med. Commun. **28**(8), 647–652 (2007).

[17]A. A. Memon *et al.*, "Positron emission tomography (PET) imaging with [llC]-labeled erlotinib: A micro-PET study on mice with lung tumor xenografts," Cancer Res. **69**(3), 873–878 (2009).

[18]J. Haller *et al.*, "Visualization of pulmonary inflammation using noninvasive fluorescence molecular imaging," J. Appl. Physiol. **104**(3), 795–802 (2008).

[19]D. Cavanaugh *et al.*, "Quantification of bleomycin-induced murine lung damage *in vivo* with micro-computed tomography," Acad. Radiol. **13**(12), 1505–1512 (2006).

[20]C. T. Badea *et al.*, "*In vivo* small-animal imaging using micro-CT and digital subtraction angiography," Phys. Med. Biol. **53**(19), R319–R350 (2008).

[21]N. L. Ford *et al.*, "*In vivo* characterization of lung morphology and function in anesthetized free-breathing mice using micro-computed tomography," J. Appl. Physiol. **102**(5), 2046–2055 (2007).

[22]C. Badea, L. W. Hedlund, and G. A. Johnson, "Micro-CT with respiratory and cardiac gating," Med. Phys. **31**(12), 3324–3329 (2004).

[23]N. L. Ford *et al.*, "Prospective respiratory-gated micro-CT of free breathing rodents," Med. Phys. **32**(9), 2888–2898 (2005).

[24]E. M. Johnson *et al.*, "A new method for respiratory gating during micro-computed tomography of lung in mice," J. Am. Assoc. Lab. Anim. Sci. **47**(4), 46–56 (2008).

[25]T. Sera *et al.*, "Development of high-resolution 4D *in vivo*-CT for visualization of cardiac and respiratory deformations of small animals," Phys. Med. Biol. **53**(16), 4285–4301 (2008).

[26]J. Hu *et al.*, "Dynamic small animal lung imaging via a postacquisition respiratory gating technique using micro-cone beam computed tomography," Acad. Radiol. **11**(9), 961–970 (2004).

[27]M. Drangova *et al.*, "Fast retrospectively gated quantitative four-dimensional (4D) cardiac micro computed tomography imaging of free-breathing mice," Invest. Radiol. **42**(2), 85–94 (2007).

[28]N. L. Ford, A. R. Wheatley, and D. W. Holdsworth, "Optimization of a retrospective technique for respiratory-gated high speed micro-CT of free-breathing rodents," Phys. Med. Biol. **51**, 5749–5769 (2007).

[29]S. H. Bartling *et al.*, "Intrinsic respiratory gating in small-animal CT,"

Eur. Radiol. **18**(7), 1375–1384 (2008).

[30]D. Ertel *et al.*, "Respiratory phase-correlated micro-CT imaging of free-breathing rodents," Phys. Med. Biol. **54**(12), 3837–3846 (2009).

[31]E. Namati *et al.*, "*In vivo* micro-CT lung imaging via a computer-controlled intermittent iso-pressure breath hold (IIBH) technique," Phys. Med. Biol. **51**(23), 6061–6075 (2006).

[32]X. Artaechevarria *et al.*, "Airway segmentation and analysis for the study of mouse models of lung disease using micro-CT," Phys. Med. Biol. **54**(22), 7009–7024 (2009).

[33]K. J. Field and C. M. Lang, "Hazards of urethane (ethyl carbamate): A review of the literature," Lab Anim. **22**(3), 255–262 (1988).

[34]G. A. Dahl, E. C. Miller, and J. A. Miller, "Comparative carcinogenicities and mutagenicities of vinyl carbamate, ethyl carbamate, and ethyl N-hydroxycarbamate," Cancer Res. **40**(4), 1194–1203 (1980).

[35]G. A. Dahl, J. A. Miller, and E. C. Miller, "Vinyl carbamate as a promutagen and a more carcinogenic analog of ethyl carbamate," Cancer Res. **38**(11), 3793–3804 (1978).

[36]R. C. Fernando *et al.*, "Detection of l,N6-ethenodeoxyadenosine and 3,N4-ethenodeoxycytidine by immunoaffinity/32P-postlabelling in liver and lung DNA of mice treated with ethyl carbamate (urethane) or its metabolites," Carcinogenesis **17**(8), 1711–1718 (1996).

[37]F. P. Guengerich and D. H. Kim, "Enzymatic oxidation of ethyl carbamate to vinyl carbamate and its role as an intermediate in the formation of l,N6-ethenoadenosine," Chem. Res. Toxicol. **4**(4), 413–421 (1991).

[38]B. Rivera *et al.*, "A novel method for endotracheal intubation of mice and rats used in imaging studies," Contemp. Top. Lab. Anim. Sci. **44**(2), 52–55 (2005).

[39]K. D. Macdonald, H. Y. Chang, and W. Mitzner, "An improved simple method of mouse lung intubation," J. Appl. Physiol. **106**(3), 984–987 (2009).

[40]M. Rivers, "Tutorial introduction to x-ray computed microtomography data processing," 1998. Available from http://www.mcs.anl.gov/research/projects/X-ray-cmt/rivers/tutorial.html.

[41]M. Boin and A. Haibel, "Compensation of ring artefacts in synchrotron tomographic images," Opt. Express **14**(25), 12071–12075 (2006).

[42]J. Sijbers and A. Postnov, "Reduction of ring artefacts in high resolution micro-CT reconstructions," Phys. Med. Biol. **49**(14), N247–N253 (2004).

[43]D. Prell, Y. Kyriakou, and W. A. Kalender, "Comparison of ring artifact correction methods for flat-detector CT," Phys. Med. Biol. **54**(12), 3881–3895 (2009).

[44]Y. Kyriakou, D. Prell, and W. A. Kalender, "Ring artifact correction for high-resolution micro CT," Phys. Med. Biol. **54**(17), N385–N391 (2009).

[45]G. T. Herman, "Correction for beam hardening in computed tomography," Phys. Med. Biol. **24**(1), 81–106 (1979).

[46]J. C. Sieren *et al.*, "A process model for direct correlation between computed tomography and histopathology: Application in lung cancer," Acad. Radiol. **17**, 169–180 (2009).

[47]L. Grady, "Random walks for image segmentation," IEEE Trans. Pattern Anal. Mach. Intell. **28**(11), 1768–1783 (2006).

[48]L. Grady *et al.*, "Random walks for interactive organ segmentation in two and three dimensions: Implementation and validation," in *Proc. Internation Conference on Medical Image Computing and Computer-Assisted Intervention (MICCAI 2005)*, Vol. 8, pp. 773–780 (2005).

[49]C. J. Zuurbier, V. M. Emons, and C. Ince, "Hemodynamics of anesthetized ventilated mouse models: Aspects of anesthetics, fluid support, and strain," Am. J. Physiol. Heart Circ. Physiol. **282**(6), H2099–H2105 (2002).

[50]T. Leal *et al.*, "Successful protocol of anaesthesia for measuring transepithelial nasal potential difference in spontaneously breathing mice," Lab Anim. **40**(1), 43–52 (2006).

[51]J. I. Cruz, J. M. Loste, and O. H. Burzaco, "Observations on the use of medetomidine/ketamine and its reversal with atipamezole for chemical restraint in the mouse," Lab Anim. **32**(1), 18–22 (1998).

[52]M. J. Daly *et al.*, "Geometric calibration of a mobile C-arm for intraoperative cone-beam CT," Med. Phys. **35**(5), 2124–2136 (2008).

[53]Y. Cho *et al.*, "Accurate technique for complete geometric calibration of cone-beam computed tomography systems," Med. Phys. **32**(4), 968–983 (2005).

[54]E. C. Holland, *Mouse Models of Human Cancer* (Wiley-Liss, Hoboken, NJ, 2004).

[55]A. M. Malkinson, "Primary lung tumors in mice as an aid for understanding, preventing, and treating human adenocarcinoma of the lung," Lung Cancer **32**(3), 265–79 (2001).

[56]N. M. De Clerck *et al.*, "High-resolution x-ray microtomography for the detection of lung tumors in living mice," Neoplasia **6**(4), 374–379 (2004).

[57]A. M. Malkinson, "Primary lung tumors in mice: An experimentally manipulate model of human adenocarcinoma," Cancer Res. **52**(9), 2670s–2676s (1992).

[58]R. H. Mole, "Quantitative observations on recovery from whole body irradiation in mice. II. Recovery during and after daily irradiation," Br. J. Radiol. **30**(349), 40–46 (1957).

[59]R. H. Mole, "Quantitative observations on recovery from whole body irradiation in mice. I. Recovery after single large doses of radiation," Br. J. Radiol. **29**(346), 563–569 (1956).

[60]A. Safwat *et al.*, "Effect of radiation dose rate and cyclophosphamide on pulmonary toxicity after total body irradiation in a mouse model," Int. J. Radiat. Oncol., Biol., Phys. **34**(1), 85–91 (1996).

[61]K. Camphausen *et al.*, "Radiation therapy to a primary tumor accelerates metastatic growth in mice," Cancer Res. **61**(5), 2207–2211 (2001).